

Investigation of Different Servo Motor Designs for Servo Cycle Operations and Loss Minimizing Control Performance

Huthaifa M. Flieh , Robert D. Lorenz, *Life Fellow, IEEE*, Eigo Totoki, Shinichi Yamaguchi, and Yuichiro Nakamura

Abstract—Servo motors are widely used in many industrial applications. These motors require precise control of acceleration, speed, and position. Different designs can be found in the literature. This paper will compare the response of two common types and will propose a new servo motor design that uses less magnet, lowering the price of the motor. The proposed motor would be able to save energy for the required application (minimize cost industrial process cost) and would be suitable for high-frequency injection based self-sensing techniques.

Index Terms—Deadbeat-direct torque and flux control (DB-DTFC), flux weakening (FW), flux intensifying (FI), field-oriented control (FOC), interior magnet permanent magnet synchronous motor (IPMSM), surface-mounted permanent magnet synchronous motor (SPMSM).

I. INTRODUCTION

SERVO motors are widely used in industrial applications that require precise control of acceleration, speed, and position. They are used in industrial robots, rolling machines, printers, etc. Servo motors require high dynamic performance. Different types of servo motors are able to serve this purpose. Permanent magnet synchronous motors (PMSMs) tend to have a high power density and high efficiency, making them the most commonly used type of servo motors.

Different PMSM designs are used for servo applications, but the two main types are the surface PMSM (SPMSM) and the interior PMSM (IPMSM). Servo motor design is optimized to achieve very low levels of ripple and cogging torque [1]. For these reasons, an IPMSM servo motor generally has low reluctance torque (low saliency ratio). The main advantage of an

Manuscript received January 6, 2018; revised April 16, 2018; accepted May 28, 2018. Date of publication June 21, 2018; date of current version October 12, 2018. Paper 2018-EMC-0017.R1, presented at the 2017 IEEE Energy Conversion Congress and Exposition, Cincinnati, OH, USA, Oct. 1–5, and approved for publication in the IEEE TRANSACTIONS ON INDUSTRY APPLICATIONS by the Electric Machines Committee of the IEEE Industry Applications Society. This work was supported by Mitsubishi Electric Corp., Amagasaki city, Hyogo, Japan. (*Corresponding author: Huthaifa M. Flieh*)

H. M. Flieh and R. D. Lorenz are with the Wisconsin Electric Machines and Power Electronics Consortium, University of Wisconsin-Madison, Madison, WI 53706 USA (e-mail: hflieh@wisc.edu; rdlorenz@wisc.edu).

E. Totoki, S. Yamaguchi, and Y. Nakamura are with Mitsubishi Electric Corporation, Amagasaki 661-0001, Japan (e-mail: Totoki.Eigo@dn.Mitsubishi.Electric.co.jp; Yamaguchi.Shinichi@dp.MitsubishiElectric.co.jp; Nakamura.Yuichiro@ak.MitsubishiElectric.co.jp).

Color versions of one or more of the figures in this paper are available online at <http://ieeexplore.ieee.org>.

Digital Object Identifier 10.1109/TIA.2018.2849725

IPMSM configuration compared to an SPMSM is that there is no need to use a sleeve for high-speed operation.

Standard IPMSMs have trackable saliency, which makes these motors suitable for injection based self-sensing control. On the other hand, standard SPMSMs have a negligible saliency, which makes this kind of motors unsuitable for self sensing. Many researchers proposed modifying the SPMSM design to create a small saliency that can be used for self-sensing control. For example, in [2], Faggion *et al.* proposed using a ringed-pole SPMSM design to create saliency. In [3], Yang *et al.* proposed using a narrow tooth tip to utilize the zigzag leakage flux, which creates a small saliency. However, the impact of these techniques on the motor power conversion was not evaluated.

The fluctuation of rare earth magnet prices in the past few years encouraged motor designers to design new motors with a smaller amount of magnetic material, reducing the price of the servo drive. Improving motor efficiency can help in reducing the industrial application operational cost.

Several PM motor designs were proposed for automotive applications, and those designs use less magnetic material in order to try to reduce the total cycle loss of the electrical drive. In [4], Prins *et al.* proposed using a flux-intensifying IPMSM (FI-IPMSM) structure for a variable gear electric vehicle drive. The authors used less magnetic material and add q -axis flux barriers to invert the motor saliency. Yan *et al.* [5] proposed an outer rotor FI-IPMSM. They claimed that their design could improve the torque under FI conditions and can operate for an extended speed range.

In [6], Limsuwan *et al.* compared the performance of self-sensing at very low-speed for flux-weakening IPMSM (FW-IPMSM) and FI-IPMSM, they claimed that the FI-IPMSM has better self-sensing performance than standard FW-IPMSMs. They showed that the FI-IPMSM achieves higher efficiency during high-speed operation, but with lower peak torque compared to the standard FW-IPMSM, which reduces total cycle loss in duty cycle traction application.

FI PM motors that can achieve the desired peak, cogging, and ripple torque requirements for servo applications have not been reported in the literature.

Many comparisons between SPMSM and IPMSM designs are found in the literature, conducted in machines for traction applications without considering the ripple and cogging torque. For example, in [7], Reddy *et al.* designed two motors, SPMSM and IPMSM, that satisfy the traction requirements. Both

TABLE I
SERVO MOTOR APPLICATION REQUIREMENTS

Specification	Requirement
cogging torque	<1.5% rated torque
torque ripple	<4% rated torque

machines achieve similar performance. However, the SPMSM has a shorter stack length and lower rated current compared to the IPMSM [SPMSM would have higher back electromotive force (EMF) for the same stack length]. A similar comparison was found in [8]. The comparison was performed in high-speed machines for automotive applications. A retaining sleeve is used in case of the SPMSM. This sleeve might not be required in the case of small-size servo motors.

A fair comparison between SPMSM and IPMSM for servo applications with very low ripple and cogging torque has not been reported in the literature.

In this paper, the SPMSM and IPMSMs will be fairly compared. The two motors were designed using the same stator, magnet, and airgap length while satisfying the servo application requirements. Then, a new servo motor design will be presented, called flux-intensifying SPMSM (FI-SPMSM). This design uses less magnetic material and its variable flux features can be used to save a significant amount of energy during the servo cycle operation. This design is also suitable for injection-based self sensing, unlike standard SPMSMs.

Section II presents a brief introduction to servo applications and servo cycles. Section III shows the finite element analysis (FEA) design procedure for both SPMSM and IPMSM rotors. Design methodology for the FI-SPMSM rotor is presented in this section. The performance of the three rotors using both FEA and experimental results is also compared in this section.

Self-sensing properties of the designed FI-SPMSM are discussed in Section IV. Section V shows the energy loss for different servo cycles for the three motors. Finally, conclusions about this paper are summarized in Section VI.

II. SERVO APPLICATIONS AND SERVO CYCLES

To achieve the required servo performance, motor designers try to design servo motors with very low cogging and ripple torque [9]. Table I summarizes typical ripple and cogging torque requirements for servo applications. Due to the extra ripple and cogging torque that is caused by manufacturing process variations, the simulated ripple and cogging torque using FEA need to be lower than the specified requirements in Table I [10]. In general, servo applications can be categorized into two main groups: point-to-point servo cycles and continuous operational servo cycles.

Point-to-point servo cycles or pick-and-place servo cycles are used in different applications like robots, printers, CNC machines, etc.; the time span of these kinds of cycles is short, often only a few seconds. A servo motor used in these kinds of cycles requires precise position control at both starting and ending points.

Continuous operational servo cycles are used in applications that require precise position and speed control all the time,

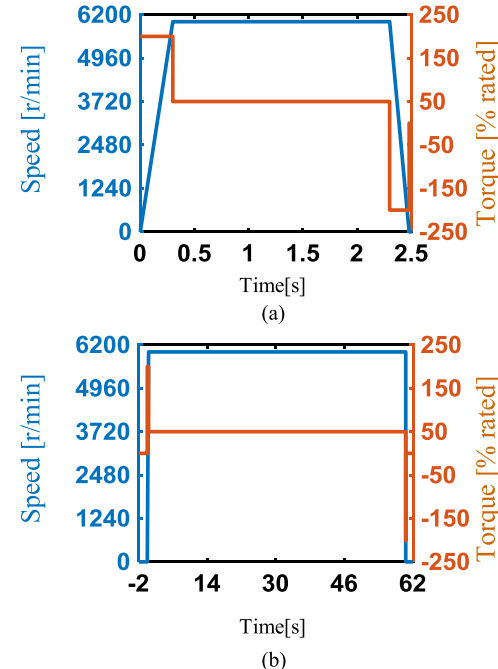


Fig. 1. Examples of servo cycles: point-to-point cycle and continuous operational cycle. (a) Point-to-point cycle. (b) Continuous operational cycle.

TABLE II
SPMSM BASELINE MOTOR SPECIFICATIONS

Specification	Value	Specification	Value
rated power	750 W	stator inner diameter	43 mm
rated torque	2.387 Nm	stator outer diameter	76.4 mm
rated speed	3000 r/min	max speed	6000 r/min
number of poles	10	number of slots	12
airgap length	0.4 mm	calculated BEMF	108 V(peak)
stack length	45 mm	rated current -rms	3.29 A

it is used in rolling machines, aluminum foil manufacturing machines, painting robots, etc.; the time span for these kinds of cycles is longer than point-to-point cycles, typically measured in minutes. Fig. 1(a) shows a sample of a point-to-point cycle, while Fig. 1(b) shows a sample of continuous operational servo cycle. In this paper, continuous operational servo cycles will be studied. Energy loss in these cycles will be compared for different servo motor designs.

III. DESIGN OF DIFFERENT PM SERVO MOTOR ROTORS USING FINITE ELEMENT ANALYSIS

The general SPMSM sizing equations found in [11]–[14] were used to obtain the initial design parameters. The airgap length is fixed at 0.4 mm (smallest feasible length). A 12-slot and 10-pole configuration is selected to achieve high winding factor (0.966) and low cogging torque [15]. Bread-loaf magnet with a parallel magnetization pattern is used in this motor, this helps in achieving a very small cogging and ripple torque [16], [17]. Table II summarizes the main characteristics and dimensions of the designed SPMSM.

Two-dimensional (2-D) FEA using JMAG Designer software was used to get the final design parameters for the SPMSM. The magnet in this motor is shaped to achieve a very low cogging and ripple torque. Fig. 2(a) shows a cross-sectional view of

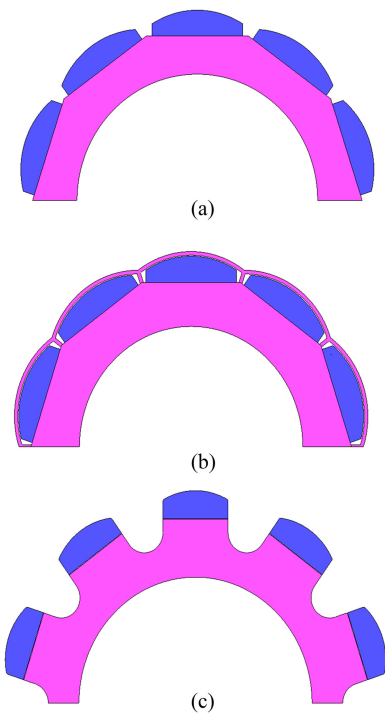


Fig. 2. Cross-sectional view of rotor design for SPMSM, IPMSM, and FI-SPMSM. (a) SPMSM. (b) IPMSM. (c) FI-SPMSM.

the designed rotor. After that, an IPMSM rotor was designed; this rotor uses the same magnet as the SPMSM rotor to reduce the manufacturing cost of this prototype rotor. To achieve low cogging and ripple torque performance, a flower-shaped IPMSM rotor configuration was used.

The airgap of the flower-shaped IPMSM is not uniform (this achieves similar reluctance in both d - q -axis directions). This is done through adding a 0.4 mm around the magnet. Fig. 2(b) shows a cross-sectional view of this rotor. This configuration minimizes the leakage flux compared to the circular shaped rotor IPMSM, which improves the torque production of the motor. Fig. 3 compares the flux lines for the flower-shaped rotor IPMSM with the circular shaped rotor IPMSM. The circular shaped rotor IPMSM has larger leakage flux, this reduces the back EMF of this motor by 18%, as shown in Fig. 4(a).

Flower-shaped IPMSM configuration helps in reducing the back EMF harmonics and achieving low ripple and cogging torque (meet the servo requirements). The flower-shaped rotor IPMSM has lower back EMF harmonics, as shown in Fig. 4(d). This motor achieves significantly lower cogging torque compared to the circular shaped rotor IPMSM, as shown in Fig. 4(b). Adding the thin iron layer on the top of the magnet in the flower-shaped IPMSM design reduces the airgap flux density by 10% compared to the SPMSM design. This can be seen in Fig. 5(a) and (b); the peak torque in the IPMSM is 10% lower than the SPMSM. This happens due to the airgap flux reduction in this motor. This difference is also shown in the measured back EMF waveform, as shown in Fig. 12.

Fig. 5(a) shows the obtained efficiency map, while Fig. 5(d) shows the iron loss map for the SPMSM. These results were obtained by using a set of correction factors that were obtained

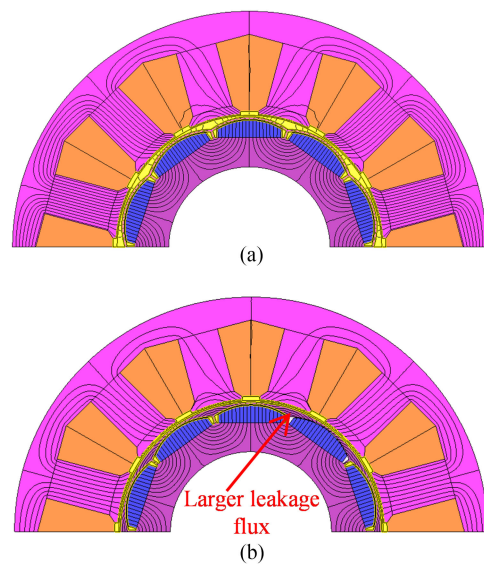


Fig. 3. Cross-sectional view and flux lines for the IPMSM using flower and circular shaped rotors. (a) Flower-shaped rotor IPMSM. (b) Circular shaped rotor IPMSM.

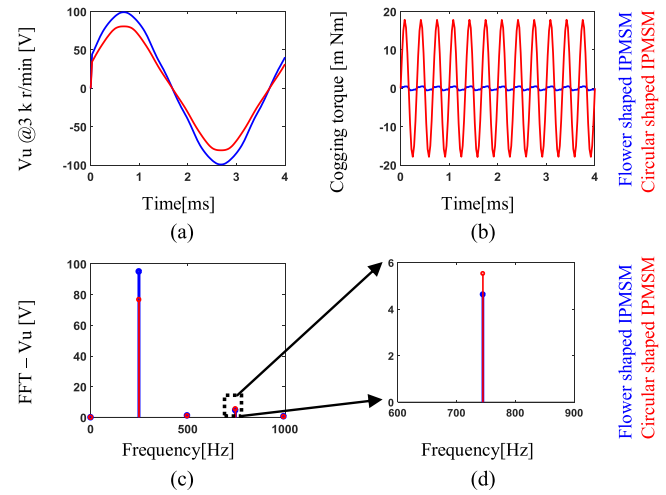


Fig. 4. Performance comparison between flower-shaped rotor IPMSM and circular shaped rotor IPMSM. (a) Back EMF. (b) Cogging torque. (c) FFT-back EMF. (d) Zoomed on (c).

from designing a similar motor and through comparing 2-D with three-dimensional (3-D) FEA simulations. These factors are summarized in Table III. These factors were used to consider the effect of end winding and leakage flux to reduce the simulation time (without using 3-D FEA to generate the maps). The efficiency and iron loss maps for the IPMSM are shown in Fig. 5(b) and (e), respectively.

The airgap flux density correction factor is obtained by comparing the calculated back EMF from 2-D FEA with 3-D FEA simulations with modeling the end winding. The inductance correction factor is used to add the leakage inductance to the 2-D calculated inductance. This factor is calculated by comparing 2-D FEA with 3-D FEA simulations. The iron loss correction factor was found by measuring the iron loss for a similar motor with the same materials (at different speed and torque

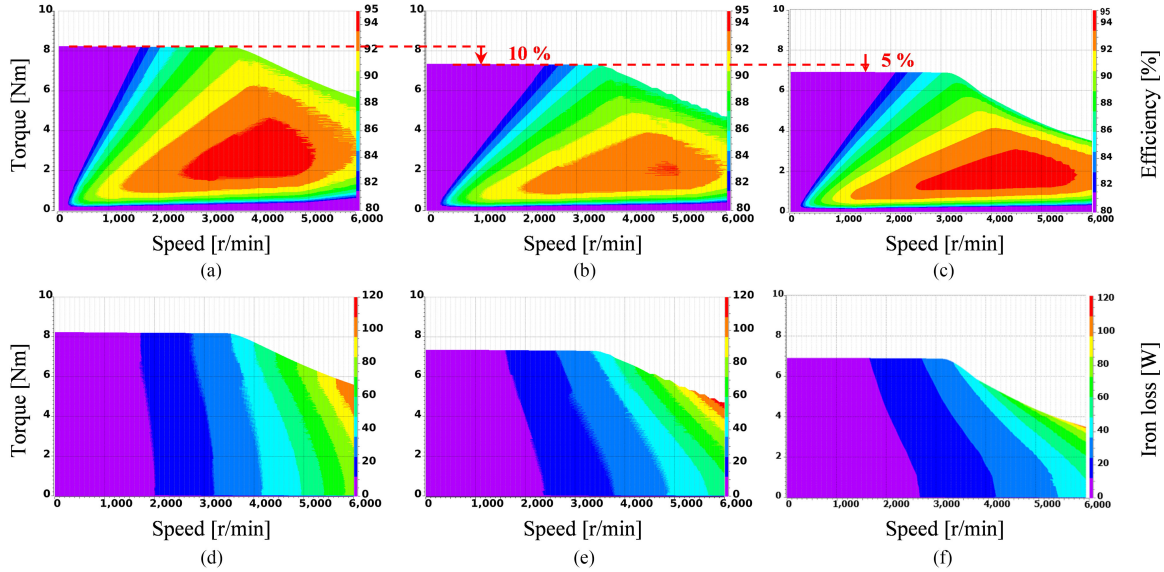


Fig. 5. Efficiency and iron loss maps for SPMSM, IPMSM, and FI-SPMSM. (a) SPMSM efficiency map. (b) IPMSM efficiency map. (c) FI-SPMSM efficiency map. (d) SPMSM iron loss map. (e) IPMSM iron loss map. (f) FI-SPMSM iron loss map.

TABLE III
CORRECTION FACTORS USED WITH 2-D FEA

Specification.	Correction factor
airgap flux density (SPMSM, IPMSM)	0.9
airgap flux density (FI-SPMSM)	0.965
inductance (SPMSM, IPMSM)	1.3
inductance (FI-SPMSM)	1.2
iron loss	2

conditions) and comparing it with the estimated loss from the 2-D FEA.

JMAG software uses the above-mentioned correction factors to adjust the current phase and amplitude, then the corresponding loss for that current is obtained from the loss lookups tables that are generated based on FEA. Iron loss correction factor is used to adjust the iron loss coefficients that are already programmed in JMAG. More information about this process can be found in the JMAG-RT help tool.

Using an SPMSM structure will maximize the air-gap flux density per magnet volume, achieving larger peak torque compared to the IPMSM configuration, as shown in Fig. 5(a) and (b). Comparing Fig. 5(d) and (e), the IPMSM rotor has lower iron loss during high-speed operation, this is due to the lower air-gap flux density compared to the SPMSM rotor. The IPMSM rotor has a small saliency ratio around 11% (this is an FW motor with $L_q > L_d$ [6]). This saliency is useful for self-sensing purposes, while the SPMSM has a negligible saliency, which makes it unsuitable for self-sensing purposes. Fig. 6(a) shows the variation of inductance with respect to the load condition for the SPMSM rotor, while Fig. 6(b) shows the same results for the IPMSM rotor. This figure also compares the measured inductances with the estimated values using 2-D FEA with correction factors. Both results show a good agreement, which verifies the used correction factors.

Combining the benefits of both IPMSM and SPMSM is possible through properly designing the FI-SPMSM. The

design procedure for the FI-SPMSM is similar to designing the FI-IPMSM, as in [5] and [6], in which the airgap flux is reduced. With that, a lower iron loss is achieved during high-speed operation, and a lower negative d -axis current is required to weaken the flux when the motor is operating at the inverter voltage limit during high-speed operation. By adding q -axis flux barriers, an inverted saliency ($L_d > L_q$) is introduced to the motor. This saliency is helpful for both self-sensing purposes and for boosting the airgap flux linkage during the peak torque operation.

Analytical equations for designing an SPMSM are still valid for the case of the FI-SPMSM. In this paper, the fundamental airgap flux density of the SPMSM was reduced by decreasing the magnet span from 162° to 110° electrical degree using (1). This is done to reduce the FW current during the high-speed operation (6000 r/min) to zero, which improves high-speed efficiency. This was done using the first harmonic assumption; Fig. 7 shows the reduction of the fundamental airgap flux density by reducing the magnet span. This will reduce the motor back EMF at 6000 r/min from 190 to $165 \text{ V}_{\Phi_{peak}}$. The maximum voltage provided by the inverter is $120 \text{ V}_{\text{peak}}$ (this is limited by the inverter dc link voltage)

$$B_g = \frac{4}{\pi} \cdot B_m \cdot \sin(\alpha) \quad (1)$$

where 2α = Magnet span (degree) corresponding to τ_m , as shown in Fig. 8.

B_m = PM flux density (tesla).

B_g = Airgap flux density (tesla).

After reducing the fundamental air-gap flux (through reducing the magnet span), an enough inverted saliency ratio ($L_d > L_q$) is added to the motor. This is done by optimizing the q -axis flux barriers and by shaping the magnet to achieve the desired cogging and ripple torque.

Multi-objective optimization using a genetic algorithm was done using MATLAB optimization engine with JMAG Designer software. A total of 30 generations with 10 population size were

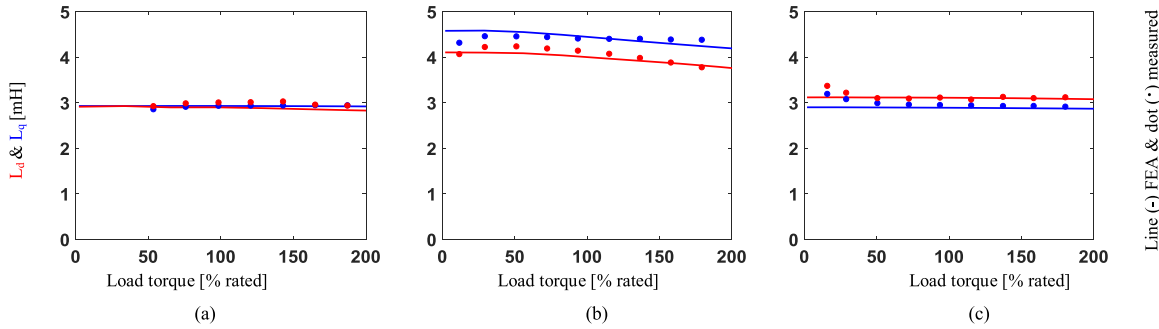


Fig. 6. Measured and simulated inductance variation with the load condition for SPMSM, IPMSM, and FI-SPMSM. (a) SPMSM. (b) IPMSM. (c) FI-SPMSM.

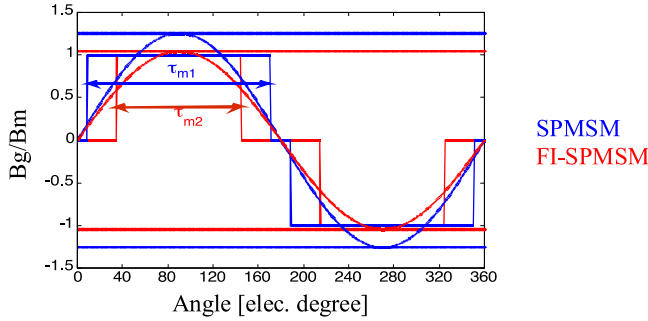


Fig. 7. Magnet span reduction to reduce the fundamental air-gap flux.

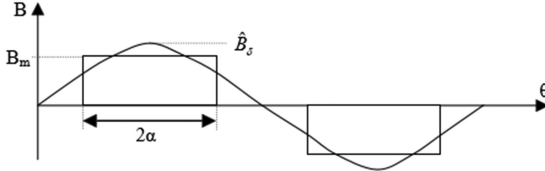


Fig. 8. Quasi-square wave and fundamental airgap flux.

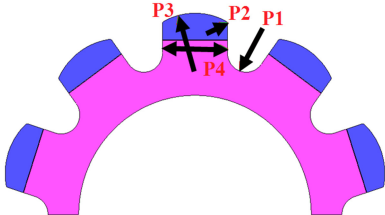


Fig. 9. Varied geometry during the optimization process for the FI-SPMSM rotor.

used. The optimization engine ran 273 cases to find the optimum solution, for every case, the current was set to zero to measure the cogging torque and to the rated current to measure the average and ripple torque, while the motor is spinning at 3000 r/min.

The optimization objectives were set to maximize the saliency ratio (L_d/L_q), maximize the average torque, limit the cogging torque to be less than 0.52%, and limit the torque ripple to be less than 3%. Fig. 9 indicates the parameters varied during the optimization process, the varied range is shown in Table IV.

Fig. 2(c) shows the cross-sectional view of the optimized FI-SPMSM rotor, while Fig. 5(c) and (f) shows the efficiency and iron loss maps for this motor. This configuration has 15%

TABLE IV
VARIED PARAMETERS DURING THE OPTIMIZATION PROCESS

Parameter	Range
q-axis flux barrier radius (p1)	1 - 2.2 mm
magnet fillet radius (p2)	0.25-1.5 mm
magnet outer radius (p3)	5 - 15 mm
magnet span (p4)	5-8 mm

TABLE V
COMPARISONS BETWEEN THE THREE DESIGNED MOTORS

Specification	SPMSM	IPMSM	FI-SPMSM
back-EMF voltage @3000 r/min (peak phase)	95V	86.5V	82.2V
PM flux (measured)	0.0623 Wb	0.0556 Wb	0.0529 Wb
rated current (measured)	3.63 A _{rms}	3.99 A _{rms}	4.2 A _{rms}
rated torque (measured)	2.38 N.m	2.38 N.m	2.38 N.m
magnet volume (FEA)	100%	100%	64%
torque ripple (FEA)	1.1%	2.5%	2.8%
cogging torque (FEA)	0.3 %	0.35%	0.51%
Saliency ratio (measured)	≈0	11%	10% (inverted)

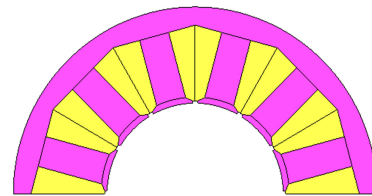


Fig. 10. Designed stator.



Fig. 11. Fabricated rotors. (left) SPMSM. (center) IPMSM. (right) FI-SPMSM.

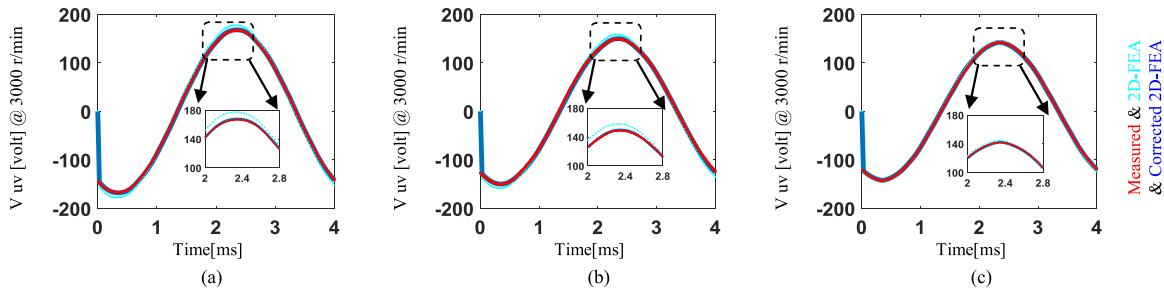


Fig. 12. Simulated and measured back EMF voltage for SPMSM, IPMSM, and FI-SPMSM. (a) SPMSM. (b) IPMSM. (c) FI-SPMSM.

lower peak torque compared to the SPMSM and 5% lower peak torque compared to the IPMSM. This is due to using a lower amount of magnetic material, but it achieves the required torque during the studied servo cycles (two times the rated torque is required during the peak acceleration period). The FI-SPMSM has a significantly lower iron loss compared to both SPMSM and IPMSM rotors, which makes this motor very efficient during medium- and high-speed operation. Fig. 6(c) shows the inductance variation for the FI-SPMSM with load variations. This motor has an inverted saliency ratio, around 10%. This saliency ratio would be useful for self-sensing purposes.

The designed FI-SPMSM uses only 64% of the magnet volume used in SPMSM or IPMSM, this will decrease the manufacturing cost of this motor from 7% to 10% (magnet cost for this size of motors is around 20–30% the total cost). This motor has slightly higher torque ripple and cogging torque compared to the SPMSM and IPMSM, but still meets the servo requirements. Table V compares the performance of the three motors using FEA and experimental evaluation.

The FI-SPMSM has 15% higher rated current compared to the SPMSM and 5% higher rated current compared to the IPMSM; thus, this motor will have higher losses during the low-speed high-torque operations when the motor copper loss is dominant. However, servo motors run at the peak torque only for a very short period during acceleration, and then run at high speed with partial load. Since the FI-SPMSM has a significantly lower iron loss during the high-speed operation, this motor can achieve a lower total motor cycle loss during the high-speed servo cycles.

In this paper, the same stator was used for evaluating the three different rotors. Fig. 10 shows the designed stator, which is a double-layer concentrated winding.

Fig. 11 shows the fabricated rotors, while Fig. 12 compares the simulated back EMF using 2-D FEA, 2-D FEA considering the correction factors and the measured one for the three rotors. The measured results match with the expected results from the FEA simulation.

The FI-SPMSM has a lower magnet leakage flux in the axial direction compared to both IPMSM and SPMSM rotors. This is due to using a shorter magnet span in the FI-SPMSM (larger gap between the magnets with larger reluctance). In the previous analysis, both SPMSM and IPMSM rotors have approximately a 10% total leakage flux. However, the FI-SPM motor has only 3.5% total leakage flux. This number is obtained by comparing the measured back EMF with the 2-D FEA simulations.

Fig. 13 shows the reluctance path for the axial leakage flux from the magnet for both SPMSM and FI-SPMSM, the air

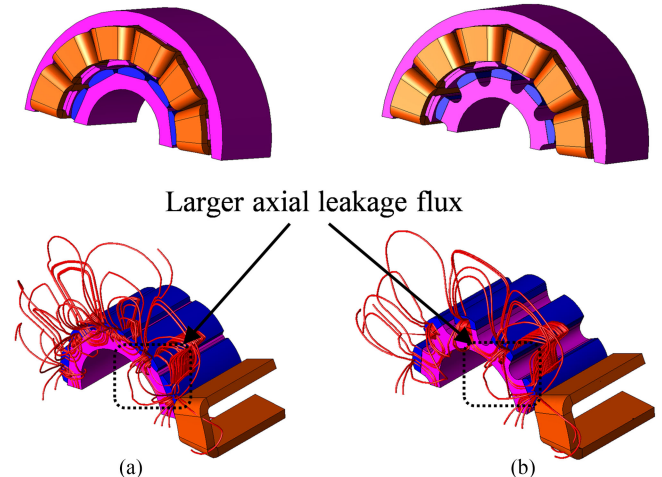


Fig. 13. 3-D model and axial magnet leakage flux for SPMSM and FI-SPMSM. (a) SPMSM. (b) FI-SPMSM.

reluctance in the axial direction for the SPMSM is smaller (magnet span is short), while in the case of the FI-SPMSM, the air reluctance in the axial direction is larger (larger distance between the magnets). This leads to lower magnet leakage flux in the axial direction for the FI-SPMSM compared to the SPMSM.

To explore the benefits of the q -axis flux barriers in the proposed FI-SPMSM rotor, the flux barriers partially filled with iron (same rotor structure like the SPMSM rotor) and the flux barriers filled with iron (inset SPMSM structure) are used, as shown in Fig. 14. Using the SPMSM rotor iron with the FI-SPMSM magnet achieves similar average torque, this motor has an inverted very small saliency (this motor has FI properties), while shaping the flux barriers in the FI-SPMSM rotor improves the saliency, allowing its use for self-sensing purposes. Fig. 15 compares the saliency ratio for these two motors at different load conditions.

The FI-SPMSM rotor is then converted to an inset SPMSM rotor through adding iron between the magnets, as shown in Fig. 14(c). The iron between the magnets provided a path for the flux to leak, affecting the torque production of the motor and decreasing the average torque by 6.6%. Fig. 16 compares the average torque for the two motors using the same excitation current.

IV. SELF-SENSING PROPERTIES OF THE DESIGNED FI-SPMSM

Self-sensing techniques are useful methods to control the motor without any physical position sensor, through using the

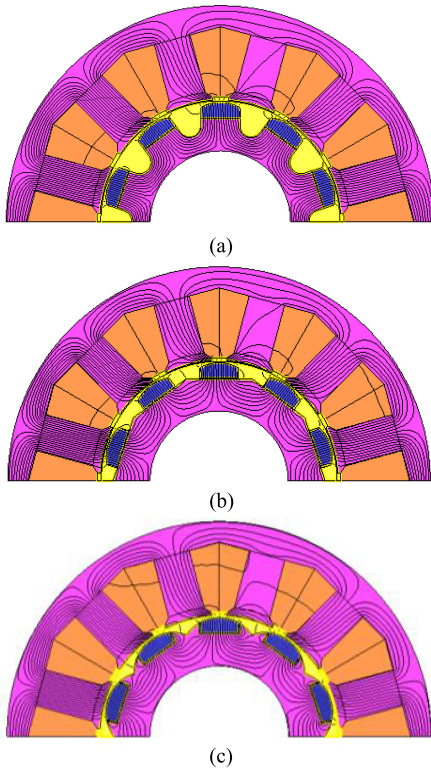


Fig. 14. Cross-sectional view of FI-SPMSM, SPMSM with a shorter magnet span and inset SPMSM. (a) FI-SPMSM. (b) SPMSM rotor iron with FI-SPMSM magnet. (c) Inset SPMSM.

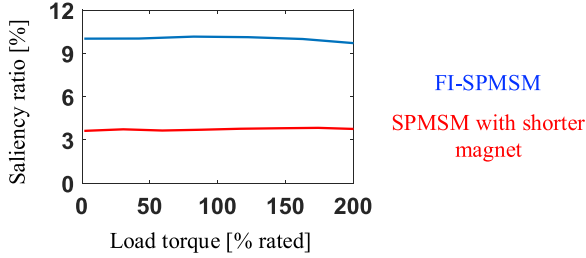


Fig. 15. Saliency ratio comparison between FI-SPMSM and SPMSM with shorter magnet span.

motor itself as a sensor. This improves the reliability of the drive and decreases the drive physical size and cost. A total of two main self-sensing techniques are used in the literature; the first one is effective for medium- and high-speed operation through tracking the motor back EMF. This method works for all electromagnetic machine types [18].

The other self-sensing technique is used to control the motor during zero and low-speed operations. This is done through tracking the motor saliency, which can be tracked by injecting a high-frequency signal on the top of the fundamental voltage and estimate the rotor position from the measured motor current without using a position sensor [19]. This method is effective in salient motors like IPMSM; however, applying these techniques to the SPMSM requires designing the motor for that purpose [2].

The FI-SPMSM is designed to have good self-sensing performance during zero and low-speed operation. The dq -axis

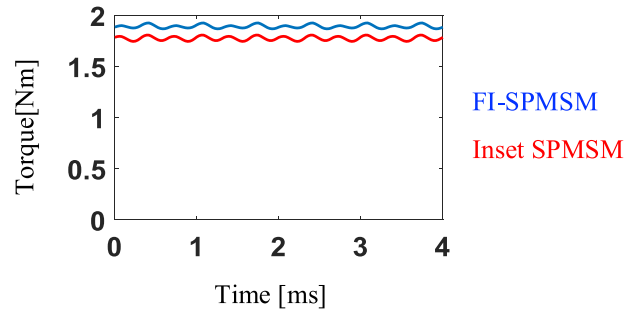


Fig. 16. Average torque comparison between FI-SPMSM and inset SPMSM.

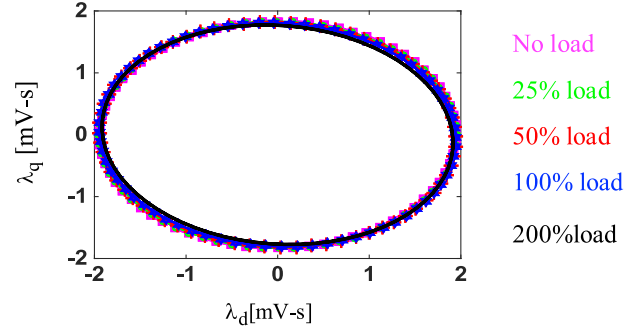


Fig. 17. Saliency image of the FI-SPMSM at different load conditions.

inductances are almost fixed with load variations. In this case, no massive inductance lookup tables are required for self-sensing control [20].

Fig. 17 shows the FI-SPMSM saliency image at different load conditions at zero speed. This image is obtained through exciting the FEA motor model with a high-frequency rotating current vector, then observing the high-frequency stator flux linkage. The motor saliency image has an elliptical shape that rotates with the motor rotor. Motor position can be estimated through comparing the observed ellipse with a predefined template, this method is called image tracking self-sensing control [21]. FI-SPMSM saliency image is fixed with load variations; this simplifies the image template for image tracking self-sensing control, in which one template can be used at different load conditions.

The accuracy of the injection based self sensing technique depends also on the angular offset of the saliency image at different load conditions [22], this happens due to the cross-saturation effect between the d - and q -axis. The angular offset of the designed FI-SPMSM motor is less than 2 electrical degrees at 200% load, which can be ignored in many applications without the need for compensation lookup table to decouple its effect. Fig. 18 shows the angular offset at different load conditions. The results of self-sensing control for the FI-SPMSM will be presented in future publications.

V. SERVO CYCLE LOSS EVALUATION AND COMPARISON OF THE DESIGNED THREE MOTORS

In this section, the energy loss in different servo cycles was measured and compared for the three fabricated rotors. In order to do so, the tested motor was connected to a commercial 3 HP

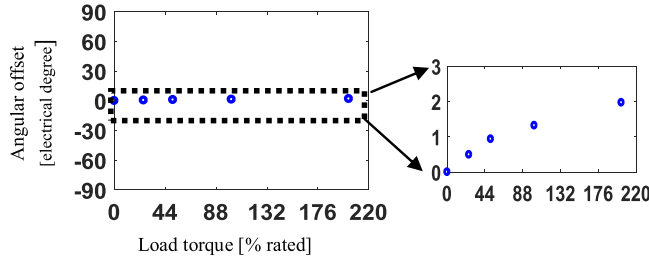


Fig. 18. Angular offset of the FI-SPMSM saliency image at different load conditions.

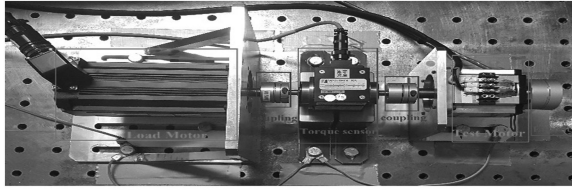


Fig. 19. Dynamometer test setup.

servo motor through a torque sensor. Fig. 19 shows the used dynamometer. A motor drive analyzer (MDA 810 from Teledyne LeCroy) was used to measure the tested motor loss.

The load motor was controlled using a field-oriented controller (FOC), while the tested motor was in motion control using loss minimizing control in deadbeat-direct torque and flux control. This controller controls the motor to operate at the optimum operating condition. More details about this controller are discussed in [23].

To evaluate the energy loss during acceleration and deceleration, the dynamic shaft torque signal is used to measure the mechanical motor power. This signal is obtained from a dynamic shaft torque observer, more details about this observer can be found in [24].

To understand the performance of the three motors, a simplified servo cycle is evaluated for the three motors. Fig. 20(a) shows the calculated speed from the encoder for the three motors, while Fig. 20(b) shows the dynamic shaft torque signal during this experiment.

Fig. 21 compares the measured dq -axis currents for the three motors for the studied cycle. The SPMSM requires lower q -axis current to generate the same torque compared to both IPMSM and FI-SPMSM, this is because this motor has the highest magnet flux (highest airgap flux density). However, the IPMSM has a very close current to the FI-SPMSM. The FI-SPMSM requires 15% higher current during the acceleration period. Since this period is very short (150–300 ms), the same size inverter can be used (inverter can be overloaded for such short periods).

The IPMSM optimum d -axis current during the 3000 r/min operation is higher than both SPMSM and FI-SPMSM to reduce the total motor loss. Both SPMSM and FI-SPMSM have similar d -axis currents; however, running the motor at a higher speed will cause the SPMSM to command a more negative d -axis current to weaken the flux when it is operating at the voltage limit. During this operation, the FI-SPMSM will achieve a lower copper loss.

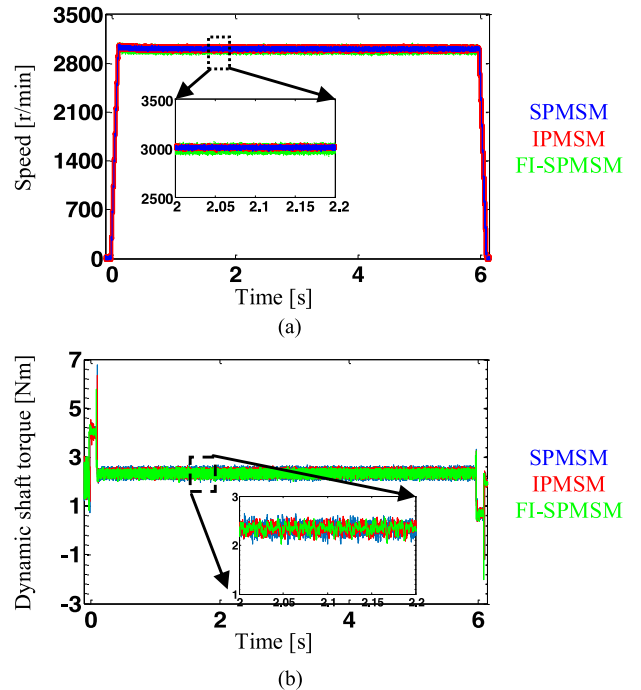


Fig. 20. Calculated speed from the encoder and estimated dynamic shaft torque for the studied simple servo cycle for the three motors. (a) Calculated speed from the encoder. (b) Observed dynamic shaft torque.

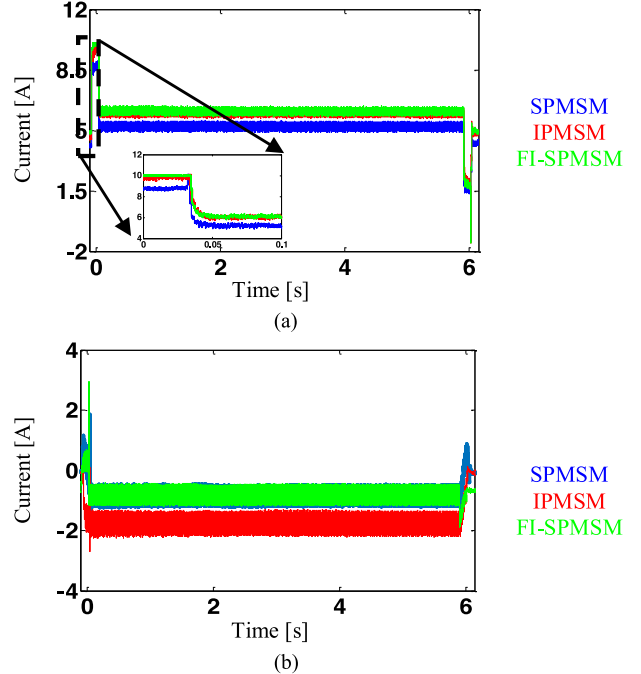


Fig. 21. Measured dq -axis current for the studied simple cycle for the three motors. (a) Measured q -axis current. (b) Measured d -axis current.

Fig. 22 shows the estimated stator flux linkage for the three motors during the same cycle. The FI-SPMSM has lower stator flux linkage than the other motors, which means lower iron loss.

Fig. 23 compares the measured loss for the three motors over the short cycle. For this cycle, the copper loss dominates the loss.

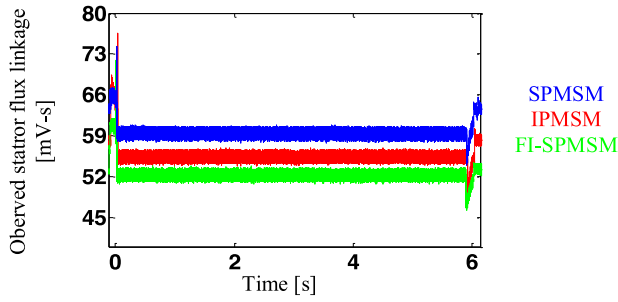


Fig. 22. Estimated stator flux linkage from the flux observer for the studied simple cycle for the three motors.

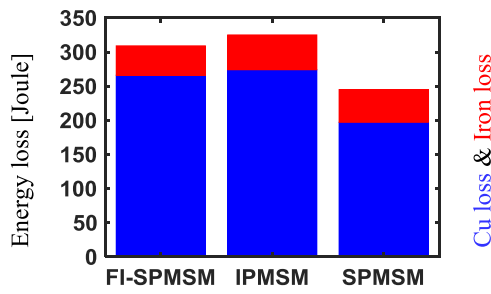


Fig. 23. Measured loss for the three rotors for the 3000 r/min short cycle.

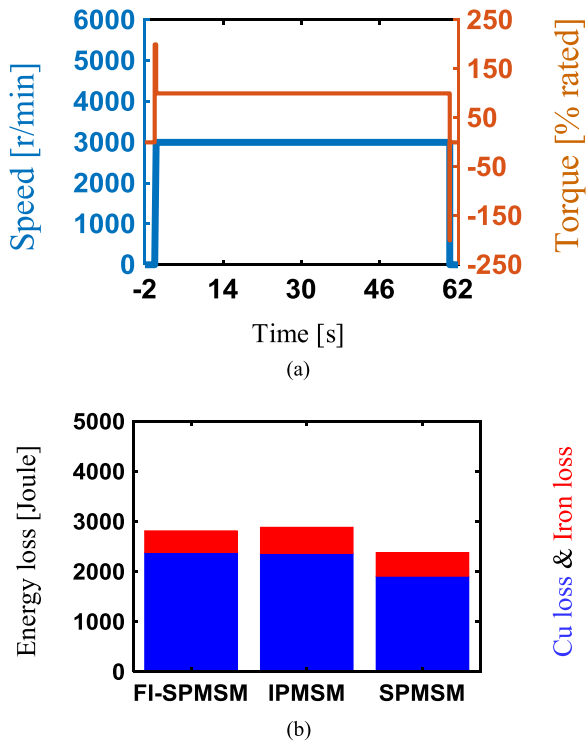


Fig. 24. Measured loss of the three rotors for the 3000 r/min continuous servo cycle. (a) 3000 r/min continuous servo cycle. (b) Measured energy loss.

For this reason, the FI-SPMSM has 28% higher losses than the SPMSM and 5% lower losses than the IPMSM.

The iron loss was measured by subtracting total motor loss from copper loss (friction and windage losses are negligible for a small-size motor).

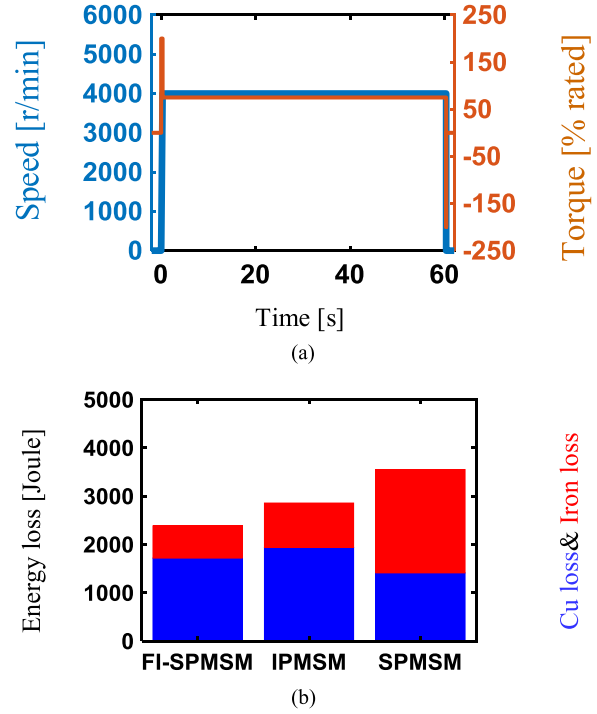


Fig. 25. Measured loss of the three rotors for the 4000 r/min continuous servo cycle. (a) 4000 r/min continuous servo cycle. (b) Measured energy loss.

Figs. 24–26 evaluate three continuous operational servo cycles. In the first cycle, the tested motor was accelerated from 0 to 3000 r/min in 150 ms, then the motor ran at 3000 r/min for 60 s. During this cycle, the rated torque (2.4 Nm) is applied using the load motor. Twice the rated torque was applied to the tested motor during the acceleration period. Loss comparison for this cycle is shown in Fig. 24. Similar to the short cycle, copper loss dominates the cycle loss. In this case, the FI-SPMSM has 28% higher losses than the SPMSM and 5% lower than the IPMSM.

In the second evaluated cycle, the tested motor was accelerated from 0 to 4000 r/min in 200 ms, then the motor ran at 4000 r/min for 60 s. During this cycle, 1.8 Nm (74% rated torque) load torque was applied using the load motor. Twice the rated torque was applied on the tested motor during the acceleration period. The copper loss for the FI-SPMSM is higher than the copper losses for the SPMSM. This is because the FI-SPMSM has lower magnet flux, so more current is required to produce the required torque. However, the iron loss is significantly lower in the FI-SPMSM compared to both the SPMSM and IPMSM. For this cycle, the FI-SPMSM has 32% lower energy loss compared to the SPMSM and 16.5% lower energy loss compared to the IPMSM; the results of this experiment are shown in Fig. 25.

Fig. 26 shows the results for the third evaluated cycle. In this cycle, the tested motor was accelerated from 0 to 4500 r/min in 225 ms, then the motor ran at 4500 r/min for 60 s. During this cycle, 1.6 Nm (66% rated torque) load torque was applied using the load motor. Twice the rated torque was applied on the tested motor during the acceleration period. Like the previous cycle, the FI-SPMSM has 40% lower energy loss compared to the SPMSM and 20% lower energy loss compared to the IPMSM.

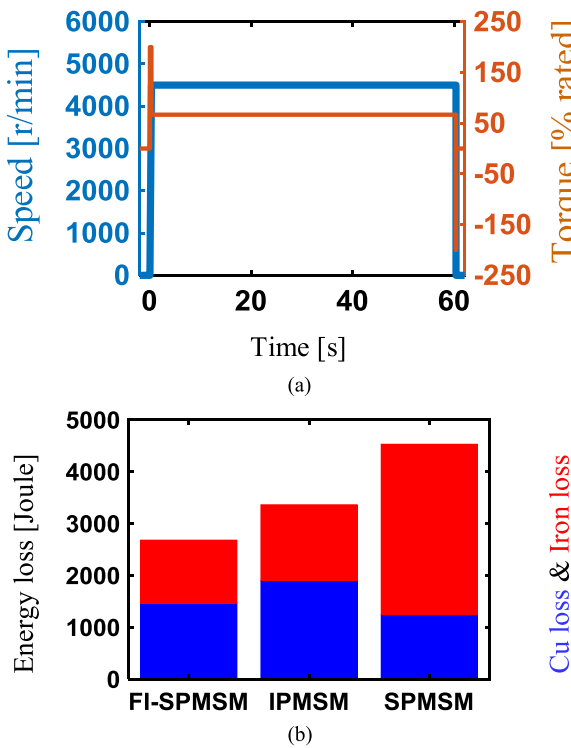


Fig. 26. Measured loss of the three rotors for the 4500 r/min continuous servo cycle. (a) 4500 r/min cycle. (b) Measured energy loss.

In previous cycles, the three motors were not operating at the voltage limit. It is expected to save more energy for higher speed cycles that operate at the voltage limit because a lower negative d -axis current is required to weaken the flux during the high-speed operation using the FI-SPMSM compared to the SPMSM. Servo cycle (the desired cycle) of 6000 r/min was not evaluated due to encoder speed limitations (maximum speed of the encoder was 4500 r/min).

VI. CONCLUSION

This paper presents a new servo motor design that uses less magnetic material compared to the standard designs. The proposed design is called the FI-SPMSM, this design has a significantly lower loss for high-speed servo cycles.

The following conclusions can be reached from the results of this paper.

- 1) The SPMSM maximizes the airgap flux density per magnet volume. While the IPMSM has lower airgap flux compared to the SPMSM, this motor achieves lower iron loss during the high-speed operation and has trackable saliency that can be used for self-sensing control.
- 2) The flower-shaped IPMSM rotor is an effective structure to reduce the magnet leakage flux in the IPMSM while satisfying the servo requirements.
- 3) The proposed FI-SPMSM combines the benefits of both SPMSM and IPMSM configurations. It maximizes the airgap flux density per magnet volume like an SPMSM, and it has low iron loss and detectable saliency like an IPMSM.

- 4) The proposed FI-SPMSM uses only 64% of the magnet volume in the SPMSM, this significantly reduces the manufacturing cost of this motor.
- 5) Copper loss dominates the cycle loss for low-speed, high-torque cycles. In these kinds of cycles, the SPMSM will have the lowest cycle loss.
- 6) Iron loss becomes significant for high-speed, low-torque cycles. In this case, the FI-SPMSM will have the lowest losses compared to SPMSM and IPMSM.
- 7) A significant amount of energy could be saved during high-speed continuous operational servo cycles if the proposed FI-SPMSM is adopted. The proposed rotor structure could save more energy for higher speed cycles when the motor is running at voltage limit operation.
- 8) The decreased thermal loading (lower cycle energy loss) could be used to enable faster acceleration or to downsize the machine, both of which are very useful outcomes for servo motor applications.

ACKNOWLEDGMENT

The authors wish to acknowledge the motivation and support provided by the Wisconsin Electric Machines and Power Electronics Consortium of the University of Wisconsin-Madison, and Mitsubishi Electric Corporation, Japan.

REFERENCES

- [1] R. Krishnan, "Selection criteria for servo motor drives," *IEEE Trans. Ind. Appl.*, vol. IA-23, no. 2, pp. 270–275, Mar. 1987.
- [2] A. Faggion, N. Bianchi, and S. Bolognani, "Ringed-pole permanent-magnet synchronous motor for position sensorless drives," *IEEE Trans. Ind. Appl.*, vol. 47, no. 4, pp. 1759–1766, Jul./Aug. 2011.
- [3] S. C. Yang, T. Suzuki, R. D. Lorenz, and T. M. Jahns, "Surface-permanent-magnet synchronous machine design for saliency-tracking self-sensing position estimation at zero and low speeds," *IEEE Trans. Ind. Appl.*, vol. 47, no. 5, pp. 2103–2116, Sep./Oct. 2011.
- [4] M. H. A. Prins, C. W. Vorster, and M. J. Kamper, "Reluctance synchronous and field intensified-PM motors for variable-gear electric vehicle drives," in *Proc. IEEE Energy Convers. Congr. Expo.*, Denver, CO, USA, 2013, pp. 657–664.
- [5] B. Yan, X. Zhu, and L. Chen, "Design and evaluation of a new flux-intensifying permanent magnet brushless motor," in *Proc. 17th Int. Conf. Electr. Mach. Syst.*, Hangzhou, China, 2014, pp. 673–677.
- [6] N. Limsuwan, Y. Shibukawa, D. D. Reigosa, and R. D. Lorenz, "Novel design of flux-intensifying interior permanent magnet synchronous machine suitable for self-sensing control at very low speed and power conversion," *IEEE Trans. Ind. Appl.*, vol. 47, no. 5, pp. 2004–2012, Sep./Oct. 2011.
- [7] P. B. Reddy, A. M. El-Refaie, K. K. Huh, J. K. Tangudu, and T. M. Jahns, "Comparison of interior and surface PM machines equipped with fractional-slot concentrated windings for hybrid traction applications," *IEEE Trans. Energy Convers.*, vol. 27, no. 3, pp. 593–602, Sep. 2012.
- [8] J. Dong, Y. Huang, L. Jin, and H. Lin, "Comparative study of surface-mounted and interior permanent-magnet motors for high-speed applications," *IEEE Trans. Appl. Supercond.*, vol. 26, no. 4, Jun. 2016, Art. no. 5200304.
- [9] P. Pillay and R. Krishnan, "Application characteristics of permanent magnet synchronous and brushless dc motors for servo drives," *IEEE Trans. Ind. Appl.*, vol. 27, no. 5, pp. 986–996, Sep./Oct. 1991.
- [10] J. Ou, Y. Liu, R. Qu, and M. Doppelbauer, "Experimental and theoretical research on cogging torque of PM synchronous motors considering manufacturing tolerances," *IEEE Trans. Ind. Electron.*, vol. 65, no. 5, pp. 3772–3783, May 2018.
- [11] G. R. Slemon, "On the design of high-performance surface-mounted PM motors," *IEEE Trans. Ind. Appl.*, vol. 30, no. 1, pp. 134–140, Jan./Feb. 1994.

- [12] D. C. Hanselman, *Brushless Permanent-Magnet Motor Design*, 1st ed. New York, NY, USA: McGraw-Hill, 1994.
- [13] J. R. Hendershot and T. J. E. Miller, *Design of Brushless Permanent-Magnet Machines*, 1st ed. Venice, FL, USA: Motor Design Books, 2010.
- [14] T. A. Lipo, *Introduction to AC Machine Design*, 1st ed. Madison, WI, USA: Wisconsin Power Electron. Res. Center, Univ. Wisconsin, 2004.
- [15] J. Cros and P. Viarouge, "Synthesis of high performance PM motors with concentrated windings," *IEEE Trans. Energy Convers.*, vol. 17, no. 2, pp. 248–253, Jun. 2002.
- [16] N. Bianchi and S. Bolognani, "Design techniques for reducing the cogging torque in surface-mounted PM motors," *IEEE Trans. Ind. Appl.*, vol. 38, no. 5, pp. 1259–1265, Sep./Oct. 2002.
- [17] S. Ruangsinchaiwanich, Z. Q. Zhu, and D. Howe, "Influence of magnet shape on cogging torque and back-emf waveform in permanent magnet machines," in *Proc. Int. Conf. Electr. Mach. Syst.*, vol. 1, 2005, pp. 284–289.
- [18] Z. Chen, M. Tomita, S. Doki, and S. Okuma, "An extended electromotive force model for sensorless control of interior permanent-magnet synchronous motors," *IEEE Trans. Ind. Electron.*, vol. 50, no. 2, pp. 288–295, Apr. 2003.
- [19] D. Raca, P. Garcia, D. D. Reigosa, F. Briz, and R. D. Lorenz, "Carrier-signal selection for sensorless control of PM synchronous machines at zero and very low speeds," *IEEE Trans. Ind. Appl.*, vol. 46, no. 1, pp. 167–178, Jan./Feb. 2010.
- [20] T. Zou, X. Han, D. Jiang, R. Qu, and D. Li, "Inductance evaluation and sensorless control of a concentrated winding PM Vernier machine," *IEEE Trans. Ind. Appl.*, vol. 54, no. 3, pp. 2175–2184, May/Jun. 2018.
- [21] T. S. Slininger, Y. Xu, and R. D. Lorenz, "Enhancing estimation accuracy by applying cross-correlation image tracking to self-sensing including evaluation on a low saliency ratio machine," in *Proc. IEEE Energy Convers. Congr. Expo.*, Milwaukee, WI, USA, 2016, pp. 1–7.
- [22] J.-H. Jang, S.-K. Sul, J.-I. Ha, K. Ide, and M. Sawamura, "Sensorless drive of surface-mounted permanent-magnet motor by high-frequency signal injection based on magnetic saliency," *IEEE Trans. Ind. Appl.*, vol. 39, no. 4, pp. 1031–1039, Jul./Aug. 2003.
- [23] H. Flieh, R. D. Lorenz, E. Totoki, S. Yamaguchi, and Y. Nakamura, "Dynamic loss minimizing control of a PM servomotor operating even at the voltage limit when using DB-DTFC," in *Proc. IEEE Energy Convers. Congr. Expo.*, Cincinnati, OH, USA, 2017, pp. 3604–3611.
- [24] H. Flieh, E. Totoki, and R. D. Lorenz, "Dynamic shaft torque observer structure enabling accurate transient loss measurements," in *Proc. IEEE Int. Electr. Mach. Drives Conf.*, Miami, FL, USA, 2017, pp. 1–8.
- [25] H. Flieh, R. D. Lorenz, E. Totoki, S. Yamaguchi, and Y. Nakamura, "Investigation of different servo motor designs for servo cycle operations and loss minimizing control performance," in *Proc. IEEE Energy Convers. Congr. Expo.*, Cincinnati, OH, USA, 2017, pp. 4316–4323.



Robert D. Lorenz (S'83–M'84–SM'91–LF'98) received the B.S.M.E., M.S.M.E.-Controls, and Ph.D.M.E.-Controls degrees from the University of Wisconsin-Madison, Madison, WI, USA, in 1969, 1970, and 1984, respectively, and the M.B.A. degree from the University of Rochester, Rochester, NY, USA, in 1980.

Since 1984, he has been on the faculty with the University of Wisconsin-Madison, where he is the Mead Witter Foundation Consolidated Papers Professor of controls engineering and a Kaiser Chair in the Department of Mechanical Engineering. He is the Co-Director of the Wisconsin Electric Machines and Power Electronics Consortium. Prior to joining the university, he worked 12 years in the industry, in Rochester, NY, on high-performance drives and synchronized motion control. He has authored more than 300 published technical papers and is the holder of 26 patents with 13 more pending.

Dr. Lorenz was the IEEE Division II Director in 2005/2006, the IEEE Industry Applications Society (IAS) President in 2001, and a Distinguished Lecturer of the IEEE IAS in 2000/2001. He was a recipient the 2003 IEEE IAS Outstanding Achievement Award, 2006 EPE Power Electronics and Motion Control Outstanding Achievement Award, 2011 IEEE IAS Distinguished Service Award, 2014 IEEE Richard H. Kaufman Technical Field Award, 2014 EPE Outstanding Achievement Award, and 34 IEEE prize paper awards on power electronics, drives, self-sensing, current regulators, motion control, etc.



Eigo Totoki received the B.S. and M.S. degrees in applied physics from The University of Tokyo, Tokyo, Japan, in 2006 and 2008, respectively.

In 2008, he joined Mitsubishi Electric Corporation Advanced Technology R&D Center, Amagasaki, Japan, and is currently a Motor Design Engineer. From 2015 to 2016, he was a Visiting Researcher with the Wisconsin Electric Machines and Power Electronics Consortium, University of Wisconsin-Madison, Madison, WI, USA. His research interests include electric motor design and control.

Mr. Totoki is a Member of the Institute of Electrical Engineers of Japan.



Shinichi Yamaguchi received the B.S. and M.S. degrees in electrical engineering from Doshisha University, Kyoto, Japan, in 1997 and 1999, respectively.

Since 1999, he has been with the Advanced Technology R&D Center, Mitsubishi Electric Corporation, Amagasaki, Japan. His main areas of research include electromechanical design and modeling of electrical machines, and magnetic material modeling.

Mr. Yamaguchi is a Member of the Institute of Electrical Engineers of Japan.



Yuichiro Nakamura received the B.S. and M.S. degrees in bio-engineering from Osaka University, Osaka, Japan, in 2010 and 2012, respectively.

In 2012, he joined Mitsubishi Electric Corporation Advanced Technology R&D Center, Amagasaki, Japan, and is currently a Motor Design Engineer. From 2017, he is working with the Servo Motor Development Section, Mitsubishi Electric Corporation Nagoya Works, Nagoya, Japan. His research interest focuses on electric motor design.

Mr. Nakamura is a Member of the Institute of Electrical Engineers of Japan.



Huthaifa M. Flieh was born in Jordan. He received the B.S. degree in electrical power engineering from Yarmouk University, Irbid, Jordan, in 2011, and the M.S. degree in sustainable transportation and electrical power systems from the University of Oviedo, Gijon, Spain, in 2014. He has been working toward the Doctorate degree in mechanical engineering at the University of Wisconsin-Madison, Madison, WI, USA, since 2014.

His research interests include electric motor design and control, focusing on loss minimization and self-sensing for servo applications.